Stability and Multiconstraint Operating Region of Grid-Connected Modular Multilevel Converter Under Grid Phase Disturbance

Yushuang Liu, *Student Member, IEEE*, Meng Huang, *Member, IEEE*, Chi K. Tse, *Fellow, IEEE*, Herbert Ho-Ching Iu, *Senior Member, IEEE*, Zhihong Yan, *Student Member, IEEE*, and Xiaoming Zha, *Member, IEEE*

***Abstract*—Grid-connected converters may operate under grid fault conditions, such as the short-/open-circuit and the transmission line switching, which may be accompanied by a phase angle difference between the grid and converter. This variation will affect the normal operation of the converter since its phase-locked loop is not able to track the grid voltage phase angle immediately. In this article, an instability phenomenon with unregulated ac line current is identified in a modular multilevel converter (MMC) based high-voltage direct-current transmission system when there is a sudden phase angle change on the grid side. A set of analytical constraints is developed for the MMC in terms of the Lyapunov stability, the modulation index, and the maximum power transfer capability. Then, a multiconstraint operating region of the MMC under various phase disturbances is derived. Moreover, the parameter influence on the operating region is analyzed and two stability-enhancing methods for the MMC system are proposed. Finally, the boundaries of the operating region and the stability-enhancing methods are verified by simulations and laboratory measurements of three-phase grid-connected MMCs.**

***Index Terms*—Grid phase disturbance, modular multilevel converter (MMC), operating region, stability analysis.**

I. Introduction

HIGH-VOLTAGE direct-current (HVdc) transmission systems play an important role in modern power grids [1]–[4]. In practical HVdc systems, the modular multilevel converter (MMC) is a widely used topology for the ac–dc conversion, thanks to its modularity, flexibility, high power capacity, and high-efficiency characteristics [5], [6]. The application of high-power MMCs has changed the characteristics of power systems to a large extent, and the operating states of the MMCs have significantly affected the safe operation of the entire power system [7]. Thus, it is of practical importance to analyze the stability of MMC-HVDC systems.

Since the MMC connects to the ac grid and suffers from various nonideal grid conditions, stability studies are widely performed in the literature. The dynamic behavior of the MMC has been shown to depend upon system parameters and control methods. In [8]–[10], impedance-based methods have been adopted to study the small-signal stability and the interaction between the weak ac grid and the MMC when the system operates with different parameters. In [11] and [12], eigenvalue analysis methods based on state-space models have been used to assess the dynamics of MMC systems with advanced controllers. However, the steady-state analysis ignores the potential phase difference between the grid voltage and the converter output.

One particular scenario is that the phase angle of grid voltage changes due to grid faults. This can be caused by short-circuits or open-circuits of ac transmission lines or line switching. During the postfault transient process, the phase-locked loop (PLL) will try to resynchronize with the ac grid. In these cases, the PLL cannot track the phase disturbance immediately because it is usually designed to have limited bandwidth to ensure system stability. Therefore, the grid-connected converter will be working with a significant phase difference with the ac grid and the converter's output voltage/current may be unregulated while a large amount of reactive current would be injected into the grid.

The existing studies are mainly focusing on the tracking performance of the PLL. The synchronization mechanism of the PLL is modeled and analyzed in [13] and [14], and the possible instability is identified considering small disturbances around its working state. Recently, the tracking performance of the PLL under large disturbances from the power grid, which can be treated as the transient stability of the system, is attracting much more attention. In [15]–[17], the transient stability of the PLL is analyzed by plotting the trajectories of the equilibrium points in power–angle curves and phase portraits. In [18], a time-domain analytical expression of the PLL is proposed and the system

Manuscript received November 17, 2020; revised March 1, 2021; accepted April 22, 2021. Date of publication May 10, 2021; date of current version July 30, 2021. This work was supported in part by the National Natural Science Foundation of China under Grants 51637007 and 51877159 and in part by Hong Kong Research Grants Council under Grant GRF 152096/17E. Recommended for publication by Associate Editor J. Liu. *(Corresponding author: Meng Huang.)*

Yushuang Liu, Meng Huang, and Xiaoming Zha are with the School of Electrical Engineering and Automation, Wuhan University, Wuhan 430072, China (e-mail: lyshuang@whu.edu.cn; meng.huang@whu.edu.cn; xmzha@whu.edu.cn).

Chi K. Tse is with the Department of Electrical Engineering, City University of Hong Kong, Hong Kong (e-mail: cktse@ieee.org).

Herbert Ho-Ching Iu is with the School of Electrical, Electronic and Computer Engineering, The University of Western Australia, Perth, WA 6009, Australia (e-mail: herbert.iu@uwa.edu.au).

Zhihong Yan is with the School of Electrical Engineering and Automation, Wuhan University, Wuhan 430072, China, and also with the Department of Electrical and Electronic Engineering, The University of Hong Kong, Hong Kong (e-mail: zhihong.y@outlook.com).

Color versions of one or more figures in this article are available at https://doi.org/10.1109/TPEL.2021.3078465.

Digital Object Identifier 10.1109/TPEL.2021.3078465

stability is assessed by calculating the PLL's output phase angle under disturbances. In [19], the energy function model of the PLL is established to derive the large-signal stability boundaries. Moreover, to tackle the instability of the PLL under grid phase disturbances, improved control methods for the PLL have been investigated. In [20], a frozen PLL structure has been studied in a conventional voltage source converter (VSC) to guarantee stability during severe faults with phase jumps. In [21], a phase jump compensation scheme of the PLL has been proposed to enhance the robustness of the PLL under grid faults, such as phase jumps without considering the structure of the converter. These studies have highlighted the risk of transient instability triggered by unstable PLLs when parameters of the PLLs are inappropriately selected or the system operates under complex grid conditions, such as faults on transmission lines, losses of generators, or large load swings in power grids [15].

However, for simplicity, the control loop is usually assumed stable during the transient process in the above-mentioned studies. It is worth noticing that the grid-connected converter may suffer from stability problems, while a stable PLL is tracking the power grid voltage disturbance. The instability, in this case, may be induced by the action of the control loop when there is a phase difference between the grid phase angle and the output phase of the PLL. For example, Tian *et al.* [22] have shown that the voltage phase jump may destroy the *dq*-axis decoupling performance of the control loop and destabilize the converter even if the PLL works normally. Actually, during the postfault tracking process, the performance of the control loop in the grid-connected MMC system is still unexplored in literature.

In view of the criticality of the abovementioned issue, this article focuses on investigating the stability of the grid-connected MMC under a grid-converter phase difference induced by a large phase disturbance. The responses of the current control, the circulating current control, and the modulation are considered while the phase disturbance occurs. In the following content, we derive the operating region of the grid-connected MMC system with current commands serving as parameters and propose effective methods to improve the stability of the MMC system under grid phase disturbances.

II. Transient Response of MMC Under Grid Phase Disturbance

Fig. 1 shows a scenario of the grid phase disturbance, which is caused by an open-circuit fault in the transmission line of the grid. For the ac power grid, assume that the voltage at the point of common coupling (PCC), $V_g\angle\theta_g$, is supported by an MMC-HVdc system and transmits through a serial transmission line $X_{\rm L}$ and two parallel transmission lines $X_{\rm line1}$ and $X_{\rm line2}$. The two parallel transmission lines are connected to an infinite bus, whose voltage is fixed at $V_{\rm bus}\angle\theta_{\rm bus}$.

With the open-circuit fault shown in Fig. 1(a), the equivalent impedance between the PCC and the infinite bus before and after the fault can be represented by X_1 and X_2 respectively, where $X_1 = X_{\rm L} + (X_{\rm line1} \parallel X_{\rm line2})$ and $X_2 = X_{\rm L} + X_{\rm line1}$. The equivalent impedance changes due to the grid fault. As the MMC-HVdc system is able to inject reactive current to support the PCC

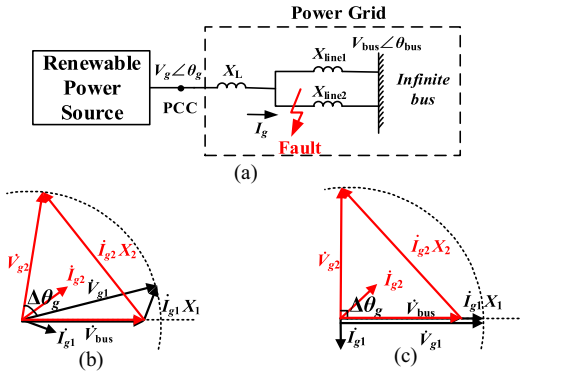

Fig. 1. Phase disturbance of power grid. (a) Circuit fault in the power grid. (b) Phasor diagram of the grid. (c) Limit case of phase jump. (Black arrows and subscript 1: prefault condition; red arrows and subscript 2: postfault condition).

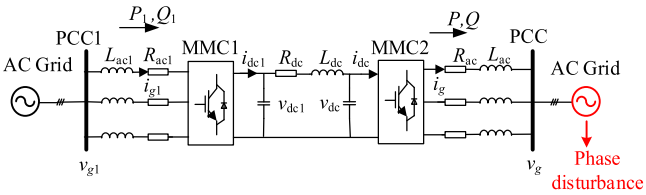

Fig. 2. Structure of the MMC-HVdc system.

voltage, the amplitude of V_g can be regarded as a constant [23]. Thus, the PCC voltage $V_g\angle\theta_{\rm g}$, which is also the grid voltage in this scenario, only varies in phase in the analysis.

When the equivalent impedance X_1 increases to X_2 due to the grid fault, the voltage drops over the equivalent impedance $I_{g2}X_2$ will be larger. Thus, the voltage phase of the power grid $\dot{V}_g$ is varied accordingly, resulting in a phase jump ($\Delta\theta_g$) of the power grid, as shown in Fig. 1(b). However, since there is no equilibrium point when the voltage phase difference between the infinite bus and the PCC exceeds 90° [15], the grid phase jump is limited accordingly, as shown in Fig. 1(c). In this case, the initial grid voltage $\dot{V}_g$ is in phase with the infinite bus voltage $\dot{V}_{\rm bus}$. After the fault, the voltage of the power grid $\dot{V}_g$ leads the infinite bus voltage $\dot{V}_{\rm bus}$ by 90°. If the postfault grid voltage phase further increases, the grid-connected system will collapse, because the system loses its equilibrium point.

In general, the MMC-HVdc system can recover to its normal operation after a slight grid phase change, thanks to the tracking ability of the PLL and the control loop, provided that the variation of grid voltage phase angle is within a certain range. However, the PLL and the control loop may fail to work if the phase change is acute.

The scenario of a three-phase 21-level MMC-HVdc system under the grid voltage phase disturbance is presented on the PSCAD/EMTDC platform. The MMC-HVdc system is shown in Fig. 2, and the topology of the MMC is presented in Fig. 3. Here, we take the MMC at the inverter side (MMC2) as an example. The parameters of MMC2 are listed in Table I. The controller of this system is given based on [24]. The commonly used *dq*-frame control loop is adopted, including an inner current

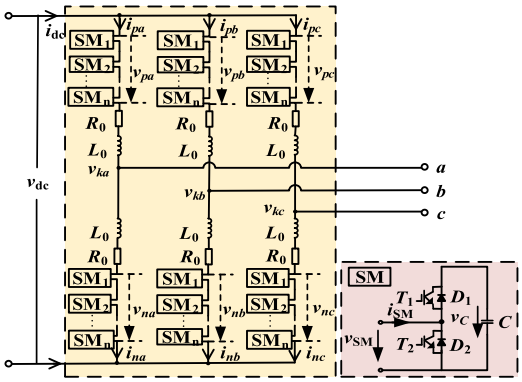

Fig. 3. Topology of a three-phase MMC.

TABLE I
SYSTEM PARAMETERS OF A THREE-PHASE 21-LEVEL MMC AT INVERTER SIDE

System Parameter	Value
Rated DC voltage V_{dc}	40 kV
Number of SMs per arm N	20
AC line resistance R_{ac}	0.1 Ω
AC equivalent inductance L_{ac}	0.1 mH
Arm inductance L_0	4 mH
Arm equivalent resistance R_0	0.1 Ω
SM capacitance C	13 mF
AC line voltage (RMS) v_g	23 kV

control loop, a circulating current control loop, and an outer power control loop, which consists of an active power loop and a reactive power loop. The capacitor voltage balancing is realized by a sorting algorithm [25]. And the modulation method is the nearest level modulation (NLM).

Typically, the PLL adjusts the output phase angle in the event of the phase variation. To simplify the analysis, the initial phase angle θ_0 before the phase variation is set as zero, and the phase angle of the grid voltage changes from θ_0 to $\theta_0 + \Delta\theta_g$ during the fault.

When the grid voltage phase angle suddenly changes to 85° at 1 s, the system enters an abnormal operating state, as shown in Fig. 4. In Fig. 4(a), the active power drops rapidly and flows in the opposite direction, while the reactive power rises excessively. The system may suffer from high current stress. From Fig. 4(b), it can be found that the PLL is still trying to track the phase angle of the ac grid voltage, although the response time could take about 100 ms [26], during which there is a phase difference between the grid voltage phase angle and the output phase of the PLL. In Fig. 4(c), the *dq*-axis current references vary dramatically as soon as the grid voltage phase angle changes. The *d*-axis reference current rises to around 280 kA immediately and exceeds the range within which the system can maintain stability. Thus, the ac current shows an overshoot and distortion phenomenon during the PLL's transient response process, as shown in Fig. 4(d).

In this article, the case under study is in such a transient process, as shown in Fig. 4. After the grid phase disturbance,

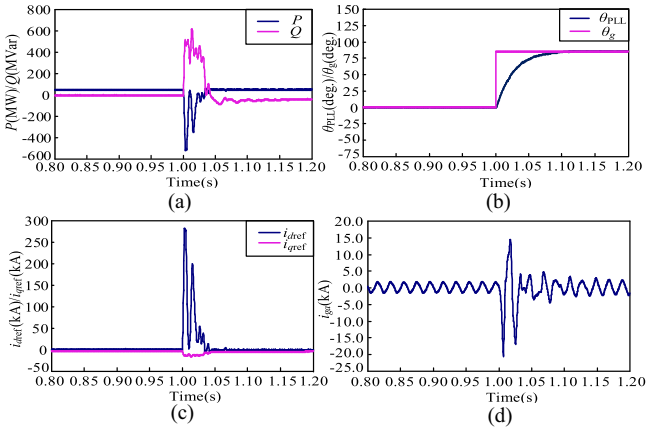

Fig. 4. Unstable phenomenon of MMC when $\Delta\theta_g = 85°$. (a) Active power and reactive power *P*/*Q*. (b) Grid and PLL output phase angle $\theta_{\mathrm{PLL}}/\theta_g$. (c) *dq*-axis reference current $i_{d\mathrm{ref}}/i_{q\mathrm{ref}}$, (d) AC current in phase a i_{ga}.

there is excessive reactive power injected into the grid-connected system, which makes the system operate with a nonunity power factor during a transient process. Besides, in the process of nonunity power factor operation shown in Fig. 4, there are two different operation modes with a stable PLL. The first one is that the phase difference between the grid voltage and the output of the PLL has not been eliminated by the tracking capability of the PLL, as shown in the response process during 1–1.1 s in Fig. 4(b). The second one is that the phase difference becomes zero after the adjustment of the PLL but the reactive power still exists in the system, as shown in the waveform after 1.1 s in Fig. 4(b). In this article, the case we focus on is similar to the process during the period from 1 to 1.1 s in Fig. 4(b) when there is a phase difference between the grid voltage and the output of the PLL after the grid disturbance.

From the simulation results, although the PLL is stable and attempts to track the variation of the grid voltage phase, the converter still injects an unregulated ac current into the power grid since the current references exceed a certain value. Then, the whole system would become unstable during the postfault transient process. Therefore, it is meaningful to investigate the operating region of the converter that operates with a phase difference between the grid voltage phase angle and the output phase of the PLL with various current command ranges. This operating region, if described in terms of a common set of practical parameters, will be highly relevant to the safe operation and the design of the internal protection for the MMC-HVdc system.

As the response time of the power loop always exceeds 100 ms, the dynamics of the power loop has little significance to the transient process within 100 ms after the grid fault. Hence, we mainly focus on the remaining part of the system including the current control loop, the circulating current control loop, and modulation. For simplicity, we maintain a fixed phase difference between the grid voltage phase angle and the output phase of the PLL by setting the output phase angle of the PLL as the initial grid phase angle before phase variation occurs. This setting is consistent with the practice since the PLL is usually designed to

be much slower than the current loops and may track the phase in several line cycles.

III. Multiconstraint Operating Regions

In order to consider the characteristics of MMCs, such as the circulating currents and the voltage ripples of submodule (SM) capacitors, we establish the model of the three-phase MMC by deriving differential equations of each harmonic component of the SM capacitor voltages and the arm currents. The circuit topology is shown in Fig. 3.

Since grid phase disturbances affect the converter by changing the *dq*-axis voltages at PCC, it is important to calculate the *dq*-axis voltages v_{gd} and v_{gq}. As mentioned earlier, the output phase angle of the PLL is kept at the value before the grid phase variation, i.e., $\theta_{\rm PLL} = \theta_g = \omega t + \theta_0$. Setting the initial phase angle of the power grid θ_0 as zero, the output phase of the PLL $\theta_{\rm PLL}$ is kept as ωt. Also, the grid phase angle after the variation can be written as $\theta_g{'} = \omega t + \theta_0 + \Delta\theta_g$. Therefore, $\Delta\theta_g$ can be regarded as the phase difference between the grid voltage phase angle and the output phase of the PLL.

Based on the *abc-dq*0 transformation matrix (1), the grid voltages in the *d*-axis and *q*-axis, denoted as v_{gd} and v_{gq}, can be calculated as (2).

$$T_\theta = \frac{2}{3}\begin{bmatrix} \cos\omega t & \cos(\omega t - 2\pi/3) & \cos(\omega t + 2\pi/3) \\ \sin\omega t & \sin(\omega t - 2\pi/3) & \sin(\omega t + 2\pi/3) \\ 1/2 & 1/2 & 1/2 \end{bmatrix} \tag{1}$$

$$\begin{cases} v_{gd} = V_m \cos(\omega t - \theta_g{'}) = V_m \cos\Delta\theta_g \\ v_{gq} = V_m \sin(\omega t - \theta_g{'}) = -V_m sin\Delta\theta_g. \end{cases} \tag{2}$$

Then, we can establish the dynamic equations of the capacitor voltages of SMs and arm currents to reflect the dynamic characteristics of the MMC. Assuming that the dc voltages of SMs in an arm are the same, an average switching model for a single arm can be described as

$$\begin{cases} C\frac{dv_{cp}}{dt} = S_p i_p \\ C\frac{dv_{cn}}{dt} = S_n i_n \end{cases} \tag{3}$$

where v_{cp} and v_{cn} represent the average capacitor voltages in the upper and the lower arm, respectively. S_p and S_n represent the average switching functions of the upper and the lower arm, i.e.,

$$\begin{cases} S_p = \frac{1}{2} - \frac{1}{2}m - \frac{v_{\rm cir}}{V_{\rm dc}} \\ S_n = \frac{1}{2} + \frac{1}{2}m - \frac{v_{\rm cir}}{V_{\rm dc}}. \end{cases} \tag{4}$$

In (4), *m* is the modulation ratio and can be calculated as $2e_v*/V_{\rm dc}$ [24], where e_v* is the output voltage of the control loop and is also the reference value of the equivalent output voltage of the MMC e_v. $v_{\rm cir}$ represents the voltage command generated by the circulating current controller.

Because the arm currents can be calculated by the dc current $i_{\rm dc}$, the ac gird current $i_{\rm g}$, and the circulating current $i_{\rm cir}$, the currents in upper and lower arms can be written as

$$\begin{cases} i_p = \frac{1}{3}i_{\rm dc} + \frac{1}{2}i_g + i_{\rm cir} \\ i_n = \frac{1}{3}i_{\rm dc} - \frac{1}{2}i_g + i_{\rm cir}. \end{cases} \tag{5}$$

From (3), (4), and (5), it can be known that the capacitor voltage v_c mainly consists of the dc component v_{c0}, the fundamental frequency component v_{c1}, the second-order component v_{c2}, and the third-order component v_{c3}, i.e.,

$$v_c = v_{c0} + v_{c1} + v_{c2} + v_{c3}. \tag{6}$$

Considering that the dc components and the second-order components in upper arms are the same as those in lower arms, and the fundamental frequency components and the third-order components in upper arms are of the opposite sign with those in lower arms, we can take the upper arm as an example to analyze the dynamics of the arm current and the SM voltage.

Substituting (4) and (5) into (3), each component of the capacitor voltage in the upper arm can be obtained [24]. Then, the differential equations of v_{c0}, v_{c1}, v_{c2}, and v_{c3} in the *dq* rotating coordinate can be expressed as eq. (7) bottom of the next page, where $e_{vd}{}^*$ and $e_{vq}{}^*$ are reference values of equivalent output voltages of the MMC e_v in the *dq*-axis.

Besides, according to the relationship between the arm voltage and the capacitor voltage, i.e., $v_p = S_p N v_{cp}$, the dc component v_{p0}, the fundamental frequency component v_{p1}, and the second-order component v_{p2} of the upper arm voltage can be derived, as shown in [24].

Then, applying KVL to the MMC inverter, the differential equations of the dc current, the ac current, and the circulating current can be calculated as

$$\begin{cases} \frac{di_{\rm dc}}{dt} = \frac{3V_{\rm dc}}{2L_0} - \frac{R_0}{L_0}i_{\rm dc} - \frac{3}{L_0}v_{p0} \\ \frac{di_g}{dt} = -\frac{R_{\rm eq}}{L_{\rm eq}}i_g - \frac{v_g}{L_{\rm eq}} - \frac{v_{p1}}{L_{\rm eq}} \\ \frac{di_{\rm cir}}{dt} = -\frac{R_0}{L_0}i_{\rm cir} - \frac{v_{p2}}{L_0} \end{cases} \tag{8}$$

where $L_{\rm eq}$ and $R_{\rm eq}$ represent the equivalent inductance $L_{\rm ac}+L_0/2$ and equivalent resistance $R_{\rm ac}+R_0/2$, respectively.

Transforming (8) into the *dq* rotating reference frame, the dynamic equations of the dc current, the *dq*-axis ac current, and the *dq*-axis circulating current are shown as eq. (9) bottom of the next page,

According to the control equation of the current control loop, $e_{vd}{}^*$ and $e_{vq}{}^*$ can be given as

$$\begin{cases} e_{vd}{}^* = v_{gd} + \omega L_{\rm eq} i_q + k_{p1}(i_{\rm dref} - i_d) + k_{i1}x_1 \\ e_{vq}{}^* = v_{gq} - \omega L_{\rm eq} i_d + k_{p1}(i_{\rm qref} - i_q) + k_{i1}x_2 \end{cases} \tag{10}$$

where $dx_1/dt = i_{\rm dref} - i_d$ and $dx_2/dt = i_{\rm qref} - i_q$. $i_{\rm dref}$ and $i_{\rm qref}$ represent the reference values of i_d and i_q, respectively. $k_{\rm p1}$ and $k_{\rm i1}$, respectively are the proportional gain and the integral gain of the current loop.

Also, the circulating current controller is designed as follows:

$$\begin{cases} v_{\rm cir2}{}_d = 2\omega L_0 i_{\rm cir2}{}_q + k_{p2}(i_{\rm cir2}{}_{\rm dref} - i_{\rm cir2}{}_d) + k_{i2}x_3 \\ v_{\rm cir2}{}_q = -2\omega L_0 i_{\rm cir2}{}_d + k_{p2}(i_{\rm cir2}{}_{\rm qref} - i_{\rm cir2}{}_q) + k_{i2}x_4 \end{cases} \tag{11}$$

where $dx_3/dt = i_{\rm cir2\,dref} - i_d$ and $dx_4/dt = i_{\rm cir2\,qref} - i_q$. $i_{\rm cir2\,dref}$ and $i_{\rm cir2\,qref}$ are always given as zero in the circulating current controller. $k_{\rm p2}$ and $k_{\rm i2}$ are the proportional gain and the integral gain of the circulating current controller.

Combining equations (2), (7), and (9)–(11), the model of the three-phase 21-level MMC with the current control loop and

circulating current control loop can be described by a set of 16 equations.

By setting state variables $x=[v_{c0}, v_{c1\,d}, v_{c1\,q}, v_{c2\,d}, v_{c2\,q}, v_{c3\,d}, v_{c3\,q}, i_{\rm dc}, i_d, i_q, i_{\rm cir2\,d}, i_{\rm cir2\,q}, x_1, x_2, x_3, x_4]^{\rm T}$, and input variables $u=[i_{d\rm ref}, i_{q\rm ref}, i_{\rm cir2\,dref}, i_{\rm cir2\,qref}, V_{\rm dc}, \Delta\theta_g]^{\rm T}$, the state-space model of the MMC can be written as $\dot{x}=f(x,u)$.

A. Lyapunov Stability Boundary

One of the main origins of the unstable operation of the MMC system is the instability of the control loops including the current control loop and the circulating current control loop. Thus, the Lyapunov method is used to assess the stability of the MMC system at a new operating point under the grid phase disturbance and derive the boundaries of the MMC system when the control loops lose stability.

To analyze the stability of the MMC at the new operating point, the equilibrium point X_Q can be solved by setting the time derivatives to zero. The Jacobian matrix $J(X_Q)$ around this equilibrium point can be derived as

$$J(X_Q)=\left.\frac{\partial f}{\partial x}\right|_{x=X_Q}=A. \tag{12}$$

Solving the characteristic equation of the system, det $|\lambda I\text{-}A|=0$, the system stability can be assessed by analyzing the signs of the real parts of eigenvalues. For a certain set of reference currents, such as the operating point when the d-axis reference current $i_{d\rm ref}$ is 2 kA and the q-axis reference current $i_{q\rm ref}$ is –10 kA, the root locus of the system as $\Delta\theta_g$ increases, as shown in Fig. 5. A pair of eigenvalues of the system when $i_{d\rm ref}=$ 2 kA and $i_{q\rm ref}=$ –10 kA will cross the imaginary axis. The root locus indicates that the system tends to be unstable with

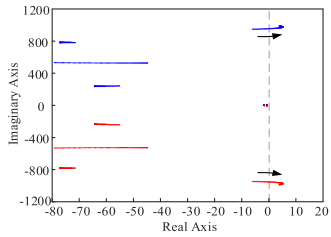

Fig. 5. Root locus with the increase of $\Delta\theta_{\rm g}$ ($0°<\Delta\theta_{\rm g}<90°$) under a certain set of dq-axis reference currents.

the increase of $\Delta\theta_g$ in the range from 0° to 90°. However, the tendency analyzed in a certain set of reference currents is not universal during the postfault transient process because the dq-axis reference currents are time varying after the grid fault. Thus, the stability of the system with all possible dq-axis reference currents under different $\Delta\theta_g$ should be analyzed.

By analyzing the eigenvalues with all possible reference currents under some phase differences, the Lyapunov stability boundaries described with the dq-axis reference currents when the phase difference is 0°, 30°, 60°, and 90° can be given to show the stability analysis results. The Lyapunov stability boundaries presented in Fig. 6 are obtained with the following steps: 1) calculating the eigenvalues with all possible reference currents under a certain $\Delta\theta_g$; 2) marking the operating points composed of $i_{d\rm ref}$ and $i_{q\rm ref}$ when the real parts of all the eigenvalues are negative in $i_{d\rm ref}$-$i_{q\rm ref}$ plane; 3) plotting the boundary of these points. It should be noted that $i_{q\rm ref}$ cannot be regarded as zero during the eigenvalue analysis because the reactive power cannot be ignored as many previous works do [8]–[12]. Comparing the Lyapunov stability boundaries when the phase difference $\Delta\theta_g$ is

$$\begin{cases}
\frac{dv_{c0}}{dt}=\frac{i_{\rm dc}}{6C}-\frac{e^*_{vd}i_d}{4CV_{\rm dc}}-\frac{e^*_{vq}i_q}{4CV_{\rm dc}}-\frac{v_{\rm cir2d}i_{\rm cir2d}}{2CV_{\rm dc}}-\frac{v_{\rm cir2q}i_{\rm cir2q}}{2CV_{\rm dc}}\\
\frac{dv_{c1d}}{dt}=-\omega v_{c1q}+\frac{i_d}{4C}-\frac{e^*_{vd}i_{\rm dc}}{3CV_{\rm dc}}-\frac{v_{\rm cir2d}i_d}{4CV_{\rm dc}}-\frac{v_{\rm cir2q}i_q}{4CV_{\rm dc}}-\frac{e^*_{vd}i_{\rm cir2d}}{2CV_{\rm dc}}-\frac{e^*_{vq}i_{\rm cir2q}}{2CV_{\rm dc}}\\
\frac{dv_{c1q}}{dt}=\omega v_{c1d}+\frac{i_q}{4C}-\frac{e^*_{vq}i_{\rm dc}}{3CV_{\rm dc}}+\frac{v_{\rm cir2d}i_q}{4CV_{\rm dc}}-\frac{v_{\rm cir2q}i_d}{4CV_{\rm dc}}+\frac{e^*_{vq}i_{\rm cir2d}}{2CV_{\rm dc}}-\frac{e^*_{vd}i_{\rm cir2q}}{2CV_{\rm dc}}\\
\frac{dv_{c2d}}{dt}=-2\omega v_{c2q}-\frac{v_{\rm cir2d}i_{\rm dc}}{3CV_{\rm dc}}+\frac{i_{\rm cir2d}}{2C}-\frac{e^*_{vd}i_d}{4CV_{\rm dc}}+\frac{e^*_{vq}i_q}{4CV_{\rm dc}}\\
\frac{dv_{c2q}}{dt}=2\omega v_{c2d}-\frac{v_{\rm cir2q}i_{\rm dc}}{3CV_{\rm dc}}+\frac{i_{\rm cir2q}}{2C}-\frac{e^*_{vd}i_q}{4CV_{\rm dc}}-\frac{e^*_{vq}i_d}{4CV_{\rm dc}}\\
\frac{dv_{c3d}}{dt}=-3\omega v_{c3q}-\frac{v_{\rm cir2d}i_d}{4CV_{\rm dc}}+\frac{v_{\rm cir2q}i_q}{4CV_{\rm dc}}-\frac{e^*_{vd}i_{\rm cir2d}}{2CV_{\rm dc}}+\frac{e^*_{vq}i_{\rm cir2q}}{2CV_{\rm dc}}\\
\frac{dv_{c3q}}{dt}=3\omega v_{c3d}-\frac{v_{\rm cir2d}i_q}{4CV_{\rm dc}}-\frac{v_{\rm cir2q}i_d}{4CV_{\rm dc}}-\frac{e^*_{vd}i_{\rm cir2q}}{2CV_{\rm dc}}-\frac{e^*_{vq}i_{\rm cir2d}}{2CV_{\rm dc}}
\end{cases} \tag{7}$$

$$\begin{cases}
\frac{di_{\rm dc}}{dt}=\frac{3V_{\rm dc}}{2L_0}-\frac{R_0}{L_0}i_{\rm dc}-\frac{3Nv_{c0}}{2L_0}+\frac{3Ne^*_{vd}v_{c1d}}{2L_0V_{\rm dc}}+\frac{3Ne^*_{vq}v_{c1q}}{2L_0V_{\rm dc}}+\frac{3Nv_{\rm cir2d}v_{c2d}}{2L_0V_{\rm dc}}+\frac{3Nv_{\rm cir2q}v_{c2q}}{2L_0V_{\rm dc}}\\
\frac{di_d}{dt}=-\omega i_q-\frac{v_{gd}}{L_{\rm eq}}-\frac{R_{eq}i_d}{L_{\rm eq}}-\frac{Nv_{c1d}}{2L_{\rm eq}}+\frac{Nv_{c0}e^*_{vd}}{L_{\rm eq}V_{\rm dc}}+\frac{Ne^*_{vd}v_{c2d}}{2L_{\rm eq}V_{\rm dc}}\\
\quad+\frac{Ne^*_{vq}v_{c2q}}{2L_{\rm eq}V_{\rm dc}}+\frac{Nv_{\rm cir2d}v_{c1d}}{2L_{\rm eq}V_{\rm dc}}+\frac{Nv_{\rm cir2q}v_{c1q}}{2L_{\rm eq}V_{\rm dc}}+\frac{Nv_{\rm cir2d}v_{c3d}}{2L_{\rm eq}V_{\rm dc}}+\frac{Nv_{\rm cir2q}v_{c3q}}{2L_{\rm eq}V_{\rm dc}}\\
\frac{di_q}{dt}=\omega i_d-\frac{v_{gq}}{L_{\rm eq}}-\frac{R_{eq}i_q}{L_{\rm eq}}-\frac{Nv_{c1q}}{2L_{\rm eq}}+\frac{Nv_{c0}e^*_{vq}}{L_{\rm eq}V_{\rm dc}}+\frac{Ne^*_{vd}v_{c2q}}{2L_{\rm eq}V_{\rm dc}}\\
\quad-\frac{Ne^*_{vq}v_{c2d}}{2L_{\rm eq}V_{\rm dc}}+\frac{Nv_{\rm cir2q}v_{c1d}}{2L_{\rm eq}V_{\rm dc}}-\frac{Nv_{\rm cir2d}v_{c1q}}{2L_{\rm eq}V_{\rm dc}}+\frac{Nv_{\rm cir2d}v_{c3q}}{2L_{\rm eq}V_{\rm dc}}-\frac{Nv_{\rm cir2q}v_{c3d}}{2L_{\rm eq}V_{\rm dc}}\\
\frac{di_{\rm cir2d}}{dt}=-2\omega i_{\rm cir2q}-\frac{R_0i_{\rm cir2d}}{L_0}-\frac{Nv_{c2d}}{2L_0}+\frac{Ne^*_{vd}v_{c1d}}{2L_0V_{\rm dc}}-\frac{Ne^*_{vq}v_{c1q}}{2L_0V_{\rm dc}}\\
\quad+\frac{Ne^*_{vd}v_{c3d}}{2L_0V_{\rm dc}}+\frac{Ne^*_{vq}v_{c3q}}{2L_0V_{\rm dc}}+\frac{Nv_{\rm cir2d}v_{c0}}{L_0V_{\rm dc}}\\
\frac{di_{\rm cir2q}}{dt}=2\omega i_{\rm cir2d}-\frac{R_0i_{\rm cir2q}}{L_0}-\frac{Nv_{c2q}}{2L_0}+\frac{Ne^*_{vq}v_{c1d}}{2L_0V_{\rm dc}}+\frac{Ne^*_{vd}v_{c1q}}{2L_0V_{\rm dc}}\\
\quad-\frac{Ne^*_{vq}v_{c3d}}{2L_0V_{\rm dc}}+\frac{Ne^*_{vd}v_{c3q}}{2L_0V_{\rm dc}}+\frac{Nv_{cir2q}v_{c0}}{L_0V_{\rm dc}}
\end{cases} \tag{9}$$

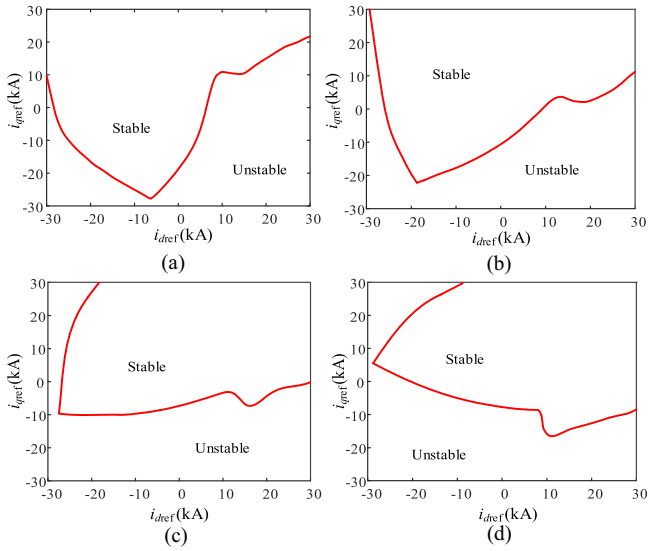

Fig. 6. Lyapunov stability boundaries with only current control and circulating current control. (a) $\Delta\theta_g = 0°$. (b) $\Delta\theta_g = 30°$. (c) $\Delta\theta_g = 60°$. (d) $\Delta\theta_g = 90°$.

equal to 0°, 30°, 60°, and 90°, as shown in Fig. 6, the Lyapunov stability boundaries tend to rotate as $\Delta\theta_g$ varies.

If the reference currents are in the unstable regions of Fig. 6, there is at least a pair of eigenvalues in the right-half plane of the complex frequency plane. The MMC will not maintain its stability due to the instability of the control loops. If the reference currents are in the stable regions, all the eigenvalues are in the left-half plane of the complex frequency plane. The control loops of the MMC will work normally. Thus, the physical meaning of the Lyapunov stability boundary is the *dq*-axis critical reference currents with which a pair of eigenvalues is on the imaginary axis when the system operates with a phase difference between the grid voltage and the PLL. Although the control loops are able to operate well in the stable regions, there is still a possibility for the MMC system to become unsafe because of other constraints.

B. Modulation Boundary

Since the switching frequency is relatively low in the MMC-HVdc system, a large number of harmonic currents will be expected when the converter enters an overmodulation region. Therefore, the modulation could be an important constraint for the system. Once the reference currents i_{dref} and i_{qref} exceed the modulation boundary, the operation mode of the system will be different.

With the increase of i_{dref} and i_{qref} after grid faults, the output reference voltages $e_{vd}*$ and $e_{vq}*$ can also grow according to the current loop control. In the NLM process, once the amplitude of the output reference voltage of the control loop $e^*_{vm} = \sqrt{{e^*_{vd}}^2 + {e^*_{vq}}^2}$ exceeds the maximum value of the output step voltage $e_{v\mathrm{NLM}}$, the MMC may operate in an overmodulation mode.

In the NLM, when ignoring the harmonic components of the capacitor voltage of SMs, $e_{v\mathrm{NLM}}$ can be given as [27]

$$e_{v\mathrm{NLM}} = \frac{4V_{c0}}{\pi}\sum_{h=1,3,5}^{\infty}\frac{1}{h}\left[\sum_{i=1}^{\frac{N}{2}}\cos(h\alpha_i)\right]\sin(h\omega t) \tag{13}$$

where V_{c0} represents the steady-state value of the dc component of SM capacitor voltages. h represents the hth harmonic component. α_i is the ith electrical angle in a quarter fundamental period, which can be obtained by [28]

$$\alpha_i = \arcsin\left[\left(i-\frac{1}{2}\right)\frac{V_{c0}}{e^*_{vm}}\right]. \tag{14}$$

Regarding the equivalent output voltage of the MMC e_v as the fundamental component of $e_{v\mathrm{NLM}}$, e_v can be written as

$$e_v = \frac{4V_{c0}}{\pi}(\cos\alpha_1 + \cos\alpha_2 + \cdots + \cos\alpha_{\frac{N}{2}})\sin\omega t. \tag{15}$$

Substituting (14) into (15), the amplitude of the equivalent output voltage of the MMC e_{vm} in the overmodulation region can be calculated as

$$e_{vm} = \frac{4V_{c0}}{\pi}\left[\sqrt{1-\left(\frac{V_{c0}}{2e^*_{vm}}\right)^2} + \sqrt{1-\left(\frac{3V_{c0}}{2e^*_{vm}}\right)^2} + \cdots + \sqrt{1-\left[\frac{(N-1)V_{c0}}{2e^*_{vm}}\right]^2}\right]. \tag{16}$$

Thus, e_{vm} may become saturated at

$$e_{vm,\mathrm{saturated}} = \lim_{e^*_{vm}\to\infty} e_{vm} = \frac{2NV_{c0}}{\pi}. \tag{17}$$

Substituting $e_{vm,\mathrm{saturated}}$ with its voltage components in the *dq*-axis, (17) can be written as

$$\sqrt{e^2_{vd,\mathrm{saturated}} + e^2_{vq,\mathrm{saturated}}} = \frac{2NV_{c0}}{\pi}. \tag{18}$$

Thus, when the system operates in an overmodulation mode, the output voltage amplitude of the current loop $e_{vm}*$ is expected to exceed the maximum value of $e_{v\mathrm{NLM}}$. This operating mode can lead to the saturation of e_{vd} and e_{vq}, as shown in (18). The saturation of e_{vd} and e_{vq} may further induce the saturation of the *dq*-axis currents i_d and i_q. If i_d and i_q cannot follow the variation of the reference currents i_{dref} and i_{qref}, the output reference voltages $e_{vd}*$ and $e_{vq}*$ may increase continuously under the influence of the current loop. As a result, positive feedback can be formed between the current loop and the modulation module, which can cause the divergence of $e_{vd}*$ and $e_{vq}*$.

When $e_{vm}*$ is far greater than $NV_{c0}/2$, the maximum value of the output step voltage $e_{v\mathrm{NLM}}$, the MMC may operate in a mode that the SMs in one arm are all connected and the SMs in the other arm of the same phase are all bypassed. The duty ratio of this mode may rise significantly until $e_{v\mathrm{NLM}}$ becomes a square wave, which may cause severe distortions of e_v.

The equivalent output voltage of the MMC inverter e_v can be calculated by $v_n/2 - v_p/2$. Considering the dc component $v_{n0} = v_{p0}$, the second-order component $v_{n2} = v_{p2}$, and ignoring harmonics in higher orders, the equivalent output voltage of

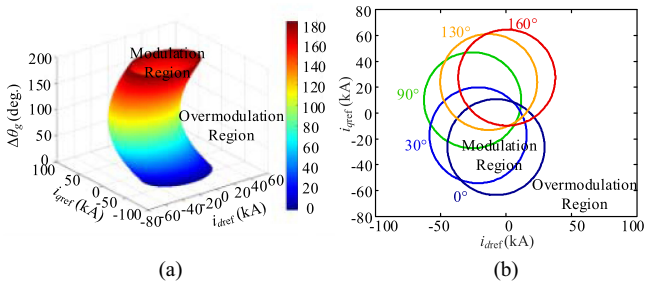

Fig. 7. Modulation boundaries of $i_{d\mathrm{ref}}$ and $i_{q\mathrm{ref}}$. (a) Modulation boundaries with a variation of $\Delta\theta_g$. (b) Modulation boundaries in the $i_{d\mathrm{ref}}$-$i_{q\mathrm{ref}}$ plane.

the MMC can be calculated as $e_v = v_{n1}/2 - v_{p1}/2 = -v_{p1}$. Substituting $-v_{p1}$ into (8) with e_v and transforming the second equation in (8) into the *dq* reference frame, we get

$$\begin{cases} L_{\mathrm{eq}}\dfrac{di_d}{dt} = e_{vd} - R_{\mathrm{eq}}i_d - v_{gd} - \omega L_{\mathrm{eq}}i_q \\ L_{\mathrm{eq}}\dfrac{di_q}{dt} = e_{vq} - R_{\mathrm{eq}}i_q - v_{gq} + \omega L_{\mathrm{eq}}i_d. \end{cases} \tag{19}$$

The saturated values of e_{vd} and e_{vq} can be calculated by (19) because the currents in the *dq* reference frame are also saturated and their time derivatives can be ignored, i.e.,

$$\begin{cases} e_{vd,\mathrm{saturated}} = v_{gd} + R_{\mathrm{eq}}i_{d,\mathrm{saturated}} + \omega L_{\mathrm{eq}}i_{q,\mathrm{saturated}} \\ e_{vq,\mathrm{saturated}} = v_{gq} + R_{\mathrm{eq}}i_{q,\mathrm{saturated}} - \omega L_{\mathrm{eq}}i_{d,\mathrm{saturated}} \end{cases} \tag{20}$$

where $i_{d,\mathrm{saturated}}$ and $i_{q,\mathrm{saturated}}$ are the saturated values of the currents in the *d* and *q* axes, respectively.

In this article, $i_{d,\mathrm{saturated}}$ and $i_{q,\mathrm{saturated}}$ are considered as the critical values below which i_d and i_q are able to follow $i_{d\mathrm{ref}}$ and $i_{q\mathrm{ref}}$. The ranges of the reference currents $i_{d\mathrm{ref}}$ and $i_{q\mathrm{ref}}$ in the modulation region can be given in (21) shown at the bottom of this page.

According to the relationship of $i_{d\mathrm{ref}}$ and $i_{q\mathrm{ref}}$ in (21), the modulation boundaries of $i_{d\mathrm{ref}}$ and $i_{q\mathrm{ref}}$ under various phase differences between the grid voltage phase angle and the output phase of the PLL are presented in Fig. 7.

As shown in Fig. 7, when there is a phase difference between the grid voltage and the PLL, if $i_{d\mathrm{ref}}$ and $i_{q\mathrm{ref}}$ are in the corresponding modulation region, the equivalent output voltage of the MMC e_v is a standard sinusoidal waveform. However, if $i_{d\mathrm{ref}}$ and $i_{q\mathrm{ref}}$ are in the overmodulation region, the amplitude of the modulation wave $e_{vm}*$ is far greater than the maximum value of the output step voltage $e_{v\mathrm{NLM}}$ so that $e_{v\mathrm{NLM}}$ may become a square wave and the equivalent output voltage of the MMC e_v will be saturated at $2NV_{c0}/\pi$. The saturation of the equivalent output voltage caused by the overmodulation will lead to the distortion of the MMC's output voltage and cause severe harmonic problems of the grid-connected system.

C. Maximum Power Transfer Boundary

In addition, since excessive active power in the system may cause high current stress and the destruction of electronic devices, the active power transferred between the power grid and the converter should be limited.

When the MMC operates in a rectifier mode, the reference currents $i_{d\mathrm{ref}}$ and $i_{q\mathrm{ref}}$ can be constrained by the maximum power, i.e.,

$$P_{\max 1} = \frac{V_{\mathrm{rms}}^2}{4R_{\mathrm{eq}}} \geq -\frac{3}{2}[v_{gd}i_{d\mathrm{ref}} + v_{gq}i_{q\mathrm{ref}} + R_{\mathrm{eq}}(i_{d\mathrm{ref}}^2 + i_{q\mathrm{ref}}^2)] \tag{22}$$

where V_{rms} is the root-mean-square (RMS) voltage of the ac grid. Moreover, when the MMC operates as an inverter, the reference currents $i_{d\mathrm{ref}}$ and $i_{q\mathrm{ref}}$ can be constrained by

$$P_{\max 2} = \frac{V_{\mathrm{dc}}^2}{4R_{\mathrm{eqDC}}} \geq \frac{3}{2}[v_{gd}i_{d\mathrm{ref}} + v_{gq}i_{q\mathrm{ref}} + R_{\mathrm{eq}}(i_{d\mathrm{ref}}^2 + i_{q\mathrm{ref}}^2)] \tag{23}$$

where $R_{\mathrm{eqDC}} = 2R_0/3$ represents the equivalent resistance at the dc side.

When the MMC operates as an inverter, the boundary constrained by the maximum power transfer capability will cover a wide range including the whole modulation region. Thus, (23) does not contribute to the final operating regions. The maximum power transfer boundaries described by $i_{d\mathrm{ref}}$ and $i_{q\mathrm{ref}}$ are mainly determined by (22). If the values of $i_{d\mathrm{ref}}$ and $i_{q\mathrm{ref}}$ exceed the maximum power transfer boundary, the power that should be transferred by the system is larger than the maximum power transfer capability, and thus, the system cannot find an equilibrium point.

D. Multiconstraint Operating Region

Combining the Lyapunov stability boundaries, the modulation boundaries, and the maximum power transfer boundaries, the comprehensive operating regions of the MMC under different phase differences can be obtained, as shown in Fig. 8. With the variation of $\Delta\theta_g$, the operation areas are different. When the reference currents $i_{d\mathrm{ref}}$ and $i_{q\mathrm{ref}}$ stay within the operation areas under different $\Delta\theta_g$, the MMC is able to operate normally. However, if the reference currents exceed any boundaries under a certain $\Delta\theta_g$, the system will fail to work owing to the instability of the control loops, the modulation limitation, or the power transfer capability.

If the phase difference between the grid voltage phase angle and the output phase of the PLL is less than 90°, the common operating region is shown in Fig. 9. The shadow area is the common stable region where the system can operate normally with any phase angle variation under 90°. When the reference currents $i_{d\mathrm{ref}}$ and $i_{q\mathrm{ref}}$ vary within the shadow area, the MMC can

$$\sqrt{(v_{gd} + R_{\mathrm{eq}}i_{d\mathrm{ref}} + \omega L_{\mathrm{eq}}i_{q\mathrm{ref}})^2 + (v_{gq} + R_{\mathrm{eq}}i_{q\mathrm{ref}} - \omega L_{\mathrm{eq}}i_{d\mathrm{ref}})^2} \leq \frac{2NV_{c0}}{\pi} \tag{21}$$

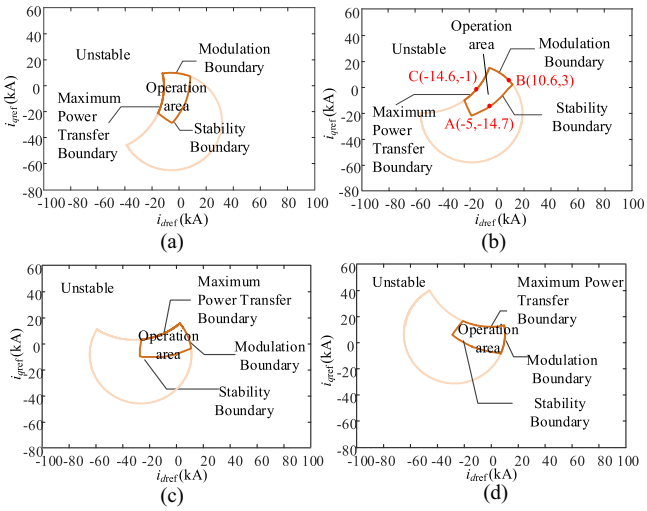

Fig. 8. Multiconstraint operating regions with variation of $\Delta\theta_g$. (a) $\Delta\theta_g = 0°$. (b) $\Delta\theta_g = 30°$. (c) $\Delta\theta_g = 60°$. (d) $\Delta\theta_g = 90°$.

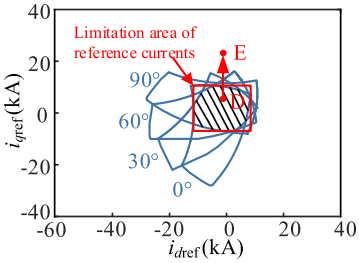

Fig. 9. Common multiconstraint operating region when $\Delta\theta_g \leq 90°$. The shadow part is the absolute safe operating region of MMC under various phase differences.

always maintain safe operation as long as the phase difference $\Delta\theta_g$ is less than 90°.

E. Comparison of Operating Region Between MMC and VSC

The operating region derivation method can be used not only in MMCs but also in two-level VSCs. However, the operating region of the VSC may be different from that of the MMC because the internal characteristics of the MMC such as the circulating current and the capacitor voltage ripples will not occur in the VSC. The comparison of the common multiconstraint operating region between the MMC and the VSC when $\Delta\theta_g \leq 90°$ is given in Fig. 10. The shadow area and the orange area represent the absolute safe operating regions of the MMC and the VSC with the same parameters under various phase differences. Comparing these two areas, the common multiconstraint operating region of the VSC includes the whole operating region of the MMC even if the equivalent parameters of these two converters are the same. It is because the Lyapunov boundaries of the MMC are reduced under the influence of the circulating current. However, the modulation boundaries and the maximum power transfer boundaries cannot be affected by the internal characteristics of the MMC. Hence, the main difference of the common operating

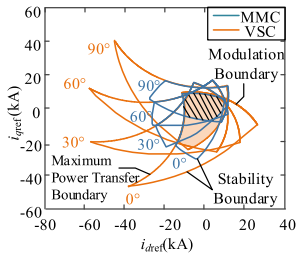

Fig. 10. Comparison of common multiconstraint operating regions between MMC and VSC when $\Delta\theta_g \leq 90°$. The orange part is the absolute safe operating region of VSC under various phase differences.

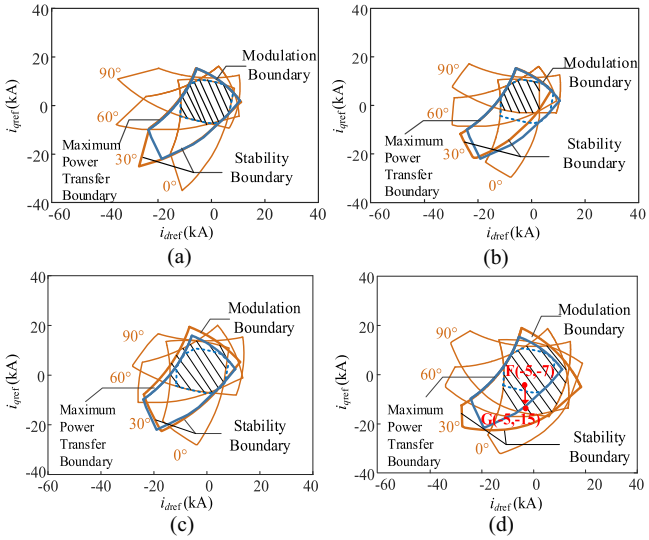

Fig. 11. Common multiconstraint operating regions with different parameters. (a) $k_{p1} = 0.2$. (b) $k_{p2} = 0.3$. (c) $R_0 = 0.05\ \Omega$. (d) $L_0 = 3$ mH.

region between the MMC and the VSC is the Lyapunov stability boundary influenced by the internal characteristics of the MMC.

IV. Parameter Influence and Stability Improvement Method

From the analysis above, it can be known that the operating region will be affected by the parameters of the MMC system. However, the way in which the operating region changes with varied parameters is still unknown. In this section, the parameter influence on the common multiconstraint operating region under phase disturbances is analyzed. Based on the parameter influence, two effective methods are proposed to enhance the stability of MMCs under grid phase disturbances.

A. Parameter Influence on Multiconstraint Operating Region

To analyze the change of the common multiconstraint operating region under different parameters, operating regions of the three-phase 21-level MMC with a different proportional gain of the current loop k_{p1}, proportional gain of the circulating current controller k_{p2}, arm resistance R_0, and arm inductance L_0 are presented in Fig. 11. The areas enclosed by blue dashed lines represent the common multiconstraint operating region with the

same parameters as Fig. 9, where $k_{p1} = 1$, $k_{p2} = 1$, $R_0 = 0.1\ \Omega$, and $L_0 = 4$ mH. The blue solid lines represent the multiconstraint operating regions when $\Delta\theta_g = 30°$, as shown in Fig. 8(b). The shadow areas enclosed by operating regions under the phase variation of 0°, 30°, 60°, and 90° are the common operating regions with a decreased parameter. From Fig. 11, it can be seen that the size of the common operating region is related to the parameters of MMC systems.

Comparing the multiconstraint operating regions with different parameters under a given phase difference (e.g., 30°), the system parameters affecting the common operating region can be identified. In Fig. 11(a), the multiconstraint operating regions with different k_{p1} when $\Delta\theta_g = 30°$ can be compared. Since a smaller proportional gain of the inner current loop k_{p1} can cause the situation that the real parts of the system eigenvalues remain negative in more operating points and improve the stability of the system, the Lyapunov boundary will become larger with a smaller k_{p1}. However, when combining multiconstraint operating regions with different $\Delta\theta_g$ under 90°, the common operating region may not be affected by k_{p1}, as shown in Fig. 11(a). Similarly, with a smaller k_{p2}, the stability boundary changes as Fig. 11(b). Combining operating regions with different $\Delta\theta_g$ under 90°, the common operating region will become smaller, as shown in Fig. 11(b). Since the arm resistance R_0 has an influence on the modulation index and the maximum power transfer capability as presented in (21) and (22), the arm resistance R_0 will change the other two boundaries, apart from the Lyapunov boundary. As shown in Fig. 11(c), the area surrounded by the maximum power transfer boundary and the modulation boundary becomes larger with a decreased R_0, and thus, the common operating region becomes larger. In Fig. 11(d), a decreased arm inductance L_0 enlarges the Lyapunov boundary and the modulation boundary, extending the common operating region. From Fig. 11, it can be found that the system will have a larger common operating region with smaller L_0, R_0 or larger k_{p2}.

Furthermore, the influences of system parameters on the different boundaries are summarized in Table II. The table shows the variation trend of different boundaries with declined system parameters. From the table, it can be concluded that the control parameters (such as k_{p1}, k_{i1}, k_{p2}, and k_{i2}) and the value of the capacitor voltage C only have an influence on the Lyapunov stability boundary of the system. Several parameters of them, such as k_{p1}, k_{i1}, k_{i2}, and C, may not affect the common multiconstraint operating region. However, other circuit parameters will change not only the Lyapunov stability boundary but also the modulation boundary and the maximum power transfer boundary. For example, the resistance parameters $R_{\rm ac}$, R_0 and the amplitude of the ac voltage V_m will have an impact on both the modulation boundary and the maximum power transfer boundary, apart from the Lyapunov boundary. The inductance parameters $L_{\rm ac}$, L_0 and the value of dc voltage $V_{\rm dc}$ will only affect the Lyapunov stability boundary and the modulation boundary. Thus, once these circuit parameters change, the common multiconstraint operating region will become different.

TABLE II
PARAMETER INFLUENCE ON DIFFERENT BOUNDARIES

Parameter	Lyapunov stability boundary	Modulation boundary	Maximum power transfer boundary	Multi-constraint operating region	Common operating region
$V_m\downarrow$	↑	↑	↓	↑	↑
$V_{\rm dc}\downarrow$	↓	↓	△	↓	↓
$R_{\rm ac}\downarrow$	↑↓	↑	↑	↑	↑
$L_{\rm ac}\downarrow$	↑	↑	△	↑	↑
$R_0\downarrow$	↑↓	↑	↑	↑	↑
$L_0\downarrow$	↑	↑	△	↑	↑
$C\downarrow$	↓	△	△	↓	△
$k_{p1}\downarrow$	↑	△	△	↑	△
$k_{i1}\downarrow$	↑	△	△	↑	△
$k_{p2}\downarrow$	↑↓	△	△	↑↓	↓
$k_{i2}\downarrow$	↓	△	△	↓	△

(↑: Extension; ↓: reduction; ↑↓: extension and reduction in different segments; △: keeping unchanged.)

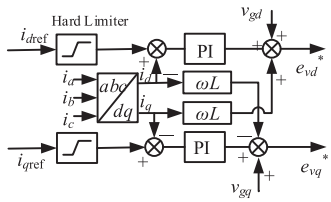

Fig. 12. Control diagram of limiting the *dq*-axis reference currents.

B. Stability Improvement Method

To enhance the stability of the system under grid phase disturbances, there are two methods proposed in this article.

The first one is to limit the values of the *dq*-axis reference currents $i_{d\rm ref}$ /$i_{q\rm ref}$ within the operating region. Adding hard limiters in the current loop can limit the increase of the reference currents effectively, as shown in Fig. 12. The limit values of $i_{d\rm ref}$ and $i_{q\rm ref}$ can be set as the maximum and minimum values of the common multiconstraint operating region. However, this method cannot eliminate the instability risks completely. As shown in Fig. 9, the red block represents the limitation area of reference currents. Although most part of the limitation area is within the common multiconstraint operating region (shadow area), there is still a small area out of the common multiconstraint operating region where the system cannot maintain stable. Thus, the method of limiting the values of the *dq*-axis reference currents $i_{d\rm ref}$ /$i_{q\rm ref}$ is not completely safe, despite of its simplicity.

The second one is to enlarge the common multiconstraint operating region. Because the size of the common multiconstraint operating region is affected by the parameters of MMC systems, adjusting the essential parameters of MMC systems appropriately can enlarge the operating region. From the conclusion of the parameter influence and the common multiconstraint operating region with different parameters shown in Fig. 11, it can be known that the stability of the grid-connected MMC system can be improved by using a smaller arm resistance R_0 or arm inductance L_0 or increasing the proportional gain of

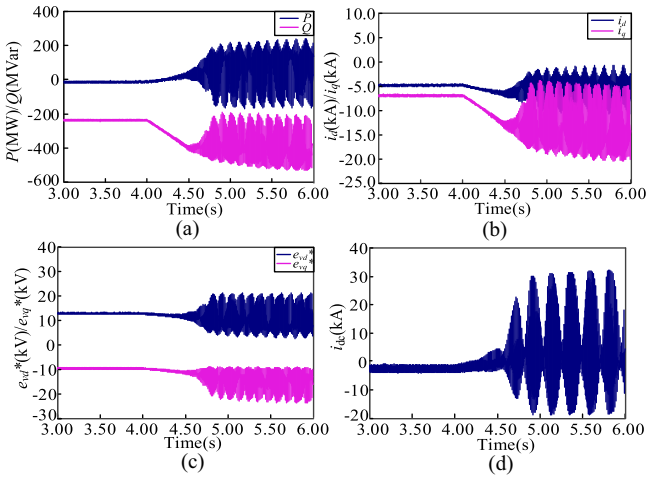

Fig. 13. Transient waveforms with i_{qref} ramping down from -7 to -15 kA when $\Delta\theta_g = 30°$. (a) Active power and reactive power *P*/*Q*. (b) *dq*-axis currents i_d/i_q. (c) *dq*-axis output voltages of current loop $e_{vd}*/e_{vq}*$. (d) DC current i_{dc}.

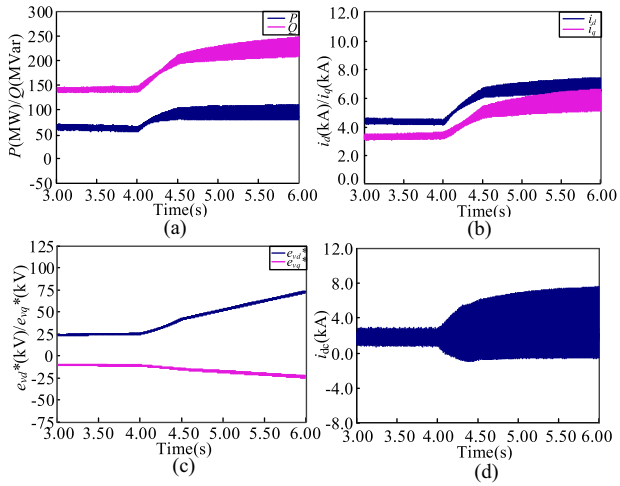

Fig. 14. Transient waveforms with i_{dref} ramping up from 5 to 17 kA when $\Delta\theta_g = 30°$. (a) Active power and reactive power *P*/*Q*. (b) *dq*-axis currents i_d/i_q. (c) *dq*-axis output voltages of current loop $e_{vd}*/e_{vq}*$. (d) DC current i_{dc}.

circulating current controller k_{p2} when there is a grid phase disturbance under 90°.

V. Simulation Verification and Controller Hardware-in-the-Loop (HIL) Test

In this section, simulations and HIL tests of various practical cases are performed to verify the multiconstraint operating regions derived in Section III.

In the simulation verification, a three-phase 21-level MMC is built on the PSCAD platform. The topology is shown in Fig. 3 and the parameters are listed in Table I. We change the reference currents to new values to simulate the outputs of the power loop after the faults. Thus, one of the *dq*-axis reference currents is set to ramp up or down at 4 s and the ramping process lasts for 0.5 s, while the other remains unchanged to keep only one variable. The operating states of the system can be identified by observing the waveforms of the active power *P*, the reactive power *Q,* the *dq*-axis currents i_d, i_q, the output voltages of the current loop $e_{vd}*$, $e_{vq}*$, and the dc current i_{dc}.

A. Lyapunov Stability Boundary Verification

Fig. 13 shows the transient responses of the MMC system with the reference currents crossing point A in Fig. 8(b) from inside to outside of the operation area when $\Delta\theta_g$ is 30°. In Fig. 13, i_{dref} is set as –5 kA and i_{qref} ramps down from –7 to –15 kA. The system can keep stable when i_{qref} is –7 kA. But when i_{qref} decreases to –15 kA, severe oscillations are observed in all the waveforms and the control loops can no longer maintain stability. As the reference currents cross point A and induce the instability of the control loops during the response process, the correctness of the Lyapunov stability boundary derived in this article can be verified.

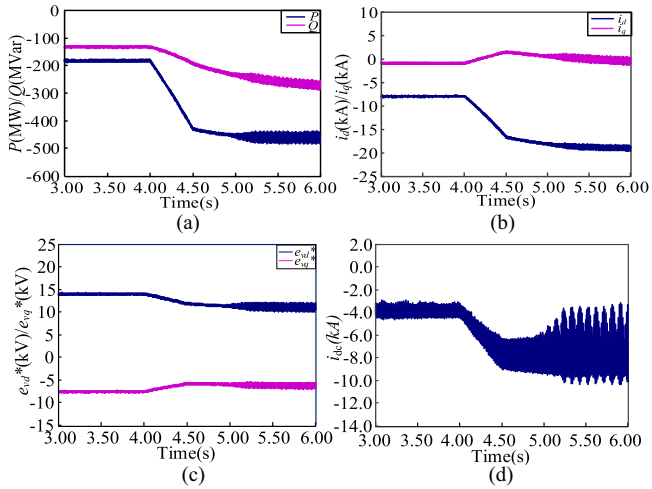

Fig. 15. Transient waveforms with i_{dref} ramping down from −8 to −19 kA when $\Delta\theta_g = 30°$. (a) Active power and reactive power *P*/*Q*. (b) *dq*-axis currents i_d/i_q. (c) *dq*-axis output voltages of current loop $e_{vd}*/e_{vq}*$. (d) DC current i_{dc}.

B. Modulation Boundary Verification

Fig. 14 shows the transient responses of the MMC system with the reference currents crossing point B in Fig. 8(b) when $\Delta\theta_g$ is 30°. In Fig. 14, i_{qref} is set as 3 kA and i_{dref} ramps up from 5 to 17 kA. When i_{dref} rises to 17 kA, $e_{vd}*$ and $e_{vq}*$ diverge constantly and the system operates in the overmodulation region. A large amount of harmonic appears in the waveforms of *P*, *Q,* and i_{dc}, and the system fails to operate safely. The simulation result is in agreement with the derived modulation boundary.

C. Maximum Power Transfer Boundary Verification

Fig. 15 shows the transient responses of the MMC system with the reference currents crossing point C in Fig. 8(b) as $\Delta\theta_g = 30°$. In Fig. 15, i_{qref} is set as –1 kA and i_{dref} ramps down from –8 to –19 kA. When i_{dref} declines to –19 kA, the system stays in

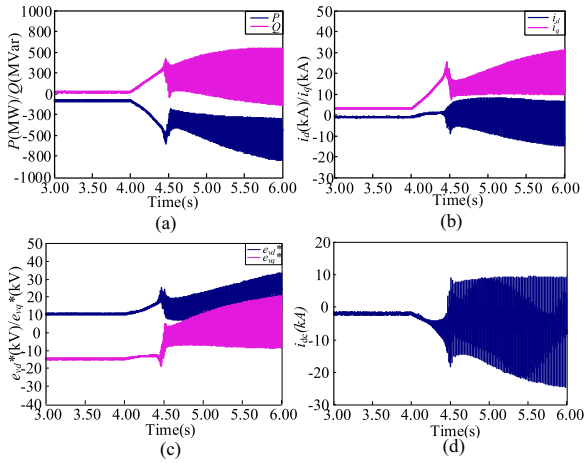

Fig. 16. Transient waveforms with i_{qref} ramping up from 3 to 23 kA and i_{dref} staying at –1 kA when $\Delta\theta_g = 60°$. (a) Active power and reactive power *P*/*Q*. (b) *dq*-axis currents i_d/i_q. (c) *dq*-axis output voltages of current loop $e_{vd}*/e_{vq}*$. (d) DC current i_{dc}.

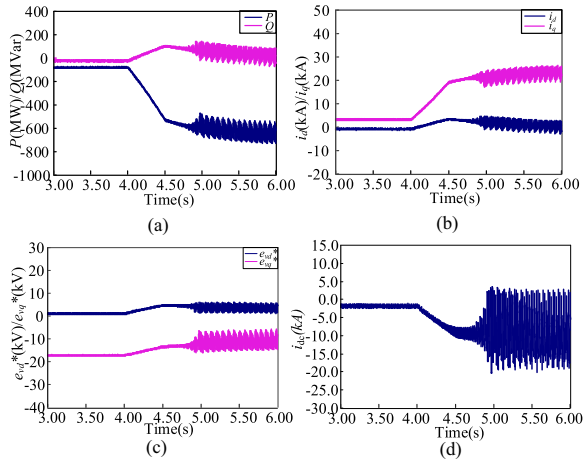

Fig. 17. Transient waveforms with i_{qref} ramping up from 3 to 23 kA and i_{dref} staying at –1 kA when $\Delta\theta_g = 90°$. (a) Active power and reactive power *P*/*Q*. (b) *dq*-axis currents i_d/i_q. (c) *dq*-axis output voltages of current loop $e_{vd}*/e_{vq}*$. (d) DC current i_{dc}.

the modulation region but the active power exceeds its maximum limit. Thus, i_{dc} cannot be maintained at the normal value. The MMC system becomes unsafe. Simulation results also verify the maximum power transfer boundary of the operating region.

D. Multiconstraint Operating Region Verification

Figs. 16 and 17 present the transient responses of the MMC with the reference currents changing from point D to E (see Fig. 9) with different values of phase disturbances (60° and 90°). In Figs. 16 and 17, when the reference currents are at point D, the system operates normally under any phase differences less than 90°. However, if the reference currents are at point E, the MMC does not work safely. Hence, it can be found that the MMC can operate well with any phase differences under 90° if the *dq*-axis reference currents are within the common multiconstraint operating region shown in Fig. 9.

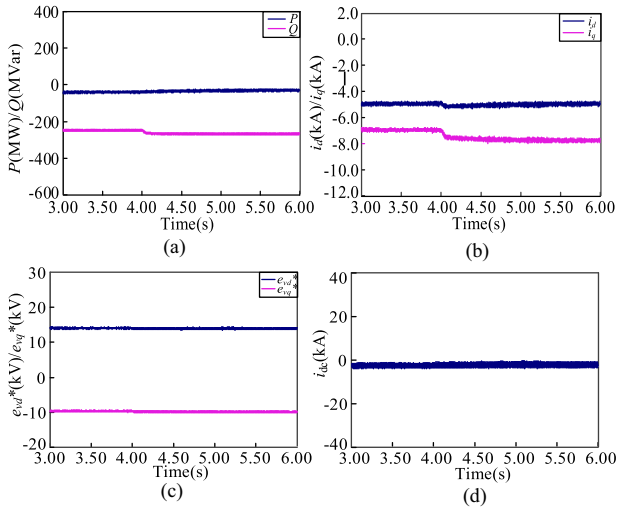

Fig. 18. Transient waveforms with input of i_{qref} ramping down from −7 to −15 kA when $\Delta\theta_g = 30°$ with hard limiters. (a) Active power and reactive power *P*/*Q*. (b) *dq*-axis currents i_d/i_q. (c) *dq*-axis output voltages of current loop $e_{vd}*/e_{vq}*$. (d) DC current i_{dc}.

E. Verification of Stability Improvement Methods

In order to validate the stability improvement methods proposed in this article, two methods are applied in MMC simulations when the parameters of the MMC system are given as the same as the parameters of Fig. 13.

First, the method of adding hard limiters in the current loop is adopted. By limiting the i_{dref} between the maximum value 7.9 kA and the minimum value −11.6 kA, and i_{qref} between 10.9 and −7.8 kA with hard limiters, the simulation with the input of i_{dref} keeping at –5 kA and the input of i_{qref} ramping down from –7 to –15 kA when $\Delta\theta_g$ is 30° is presented in Fig. 18. Comparing the results of Figs. 13 and 18, it can be seen that the MMC system is able to maintain stability under the phase difference with hard limiters in the current loop.

To verify the parameter influence on the common operating region and the stability improvement method of enlarging the operating region, a simulation of a 21-level MMC system with a smaller arm inductance (3 mH) is performed as an example when there is a phase disturbance of 30°. The reference currents of the system change from point F to G, as shown in Fig. 11(d). From the simulation result shown in Fig. 19, we can know the system can operate normally and the result is in agreement with the analysis result in Fig. 11(d). Besides, Fig. 13 shows the MMC system with a 4 mH arm inductance loses stability when the system operates from point F to G. Thus, by comparison of the results in Figs. 13 and 19, it can be known that the stability of the MMC system can be improved with a smaller arm inductance.

F. Controller Hardware-in-the-Loop Test

In many recent publications [19], [29], controller HIL tests for complex power electronic converters have been used for verifying the stability, operation, and fault tolerance of grid-connected converter systems. By interfacing the hardware controller with emulated power electronic circuits, researchers can

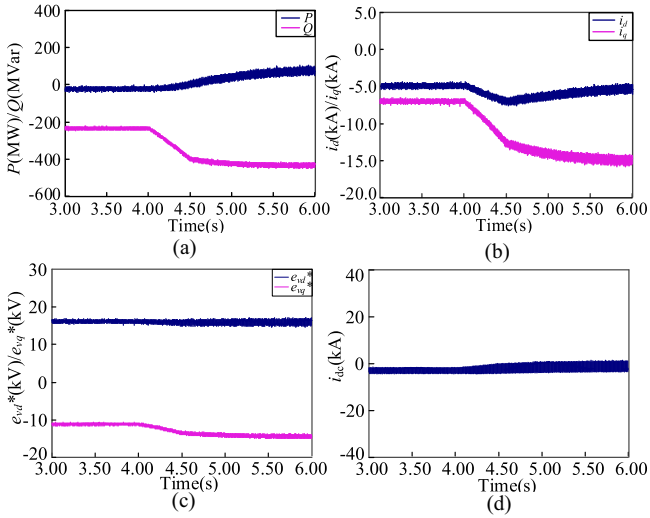

Fig. 19. Transient waveforms with $i_{q\mathrm{ref}}$ ramping down from -7 to -15 kA when $\Delta\theta_g = 30°$ with a smaller inductance. (a) Active power and reactive power P/Q. (b) dq-axis currents i_d/i_q. (c) dq-axis output voltages of current loop $e_{vd}*/e_{vq}*$. (d) DC current i_{dc}.

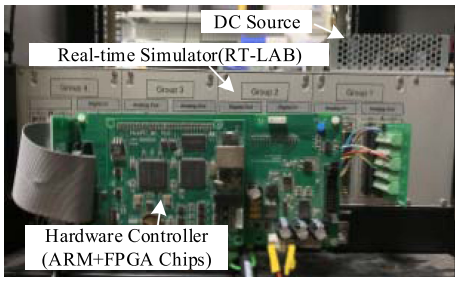

Fig. 20. HIL test platform of the three-phase five-level MMC.

TABLE III
SYSTEM PARAMETERS OF A THREE-PHASE FIVE-LEVEL MMC

System Parameter	Value
Rated DC voltage V_{dc}	8000 V
Number of SMs per arm N	4
AC line resistance R_{ac}	0.2 Ω
AC equivalent inductance L_{ac}	1 mH
Arm inductance L_0	4 mH
Arm equivalent resistance R_0	0.1 Ω
SM capacitance C	2.6 mF
AC line voltage v_g	4600 V

easily test the operation of the system without necessarily building a downscaled system mockup. A controller HIL test of a three-phase five-level MMC is conducted to further validate the operating region analyzed in Section III. In the HIL test, the circuit model of the three-phase five-level MMC is established on the RT-LAB platform, and the control is realized by the hardware controller (STM32F401) with an FPGA (EP4CE115F23C7). The HIL test platform of the three-phase five-level MMC is shown in Fig. 20, and the parameters of the three-phase five-level MMC are listed in Table III.

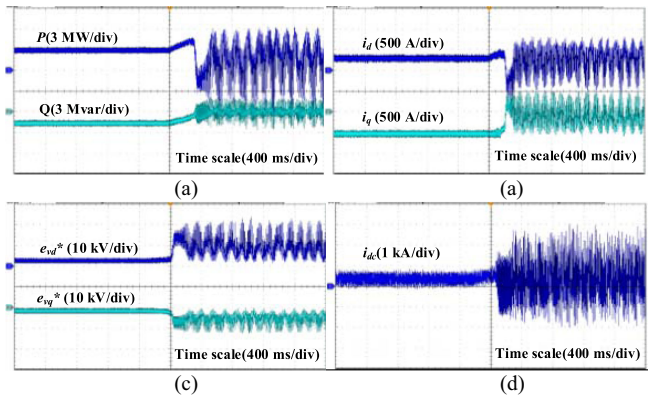

Fig. 21. HIL test verification of the multiconstraint operating region ($k_{p2} = 0.4$). (a) Active power and reactive power P/Q. (b) dq-axis currents i_d/i_q. (c) dq-axis output voltages of current loop $e_{vd}*/e_{vq}*$. (d) DC current i_{dc}.

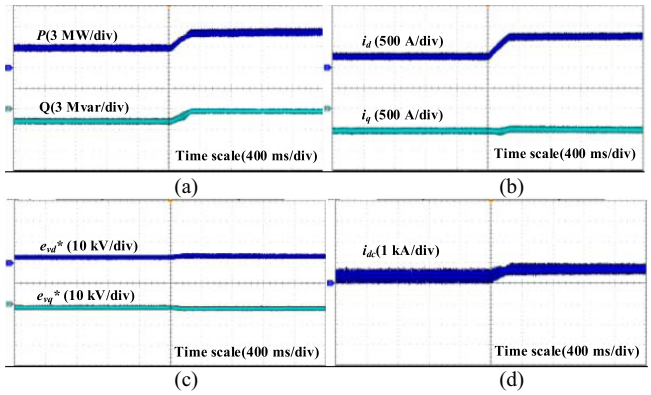

Fig. 22. HIL test verification of the parameter influence ($k_{p2} = 2$). (a) Active power and reactive power P/Q. (b) dq-axis currents i_d/i_q. (c) dq-axis output voltages of current loop $e_{vd}*/e_{vq}*$. (d) DC current i_{dc}.

The phase difference between the grid voltage phase angle and the output phase of the PLL is set as 30°. The q-axis reference current $i_{q\mathrm{ref}}$ stays at -500 A, while the d-axis reference current $i_{d\mathrm{ref}}$ is set to ramp up from 300 A at 2 s to 900 A at 2.3 s (crossing the Lyapunov stability boundary $i_{\mathrm{dref}} = 476$ A). The transient waveforms are shown in Fig. 21. When $i_{d\mathrm{ref}}$ exceeds 476 A, the active power P, the reactive power Q, the dq-axis currents i_d and i_q, and the dq-axis reference voltages $e_{vd}*$ and $e_{vq}*$ start to oscillate, showing that the control loops become unstable when the operation point moves outside of the multiconstraint operating region. The MMC cannot maintain stability with this set of parameters when the phase difference is 30°. From these waveforms, the derived operating area in Section III can be further verified.

To enhance the stability of the MMC, the proportional gain of the circulating current loop k_{p2} is increased to 2, while the gain k_{p2} is 0.4 in Fig. 21. The stable responses of the MMC with $i_{q\mathrm{ref}}$ keeping at -500 A and $i_{d\mathrm{ref}}$ ramping up from 300 to 900 A when the phase difference is 30° are presented in Fig. 22. Comparing Figs. 21 and 22, we can know that the stability can be improved by rising the proportional gain of the circulating

current loop k_{p2}. The HIL test result is in agreement with the parameter influence analysis in Section IV.

VI. Conclusion

In HVdc transmission systems, grid phase disturbances may lead to excessive currents and affect the operation of the systems. Thus, the identification of stable operating regions of converters described with reference currents is indispensable for the safe operation of MMC-HVdc systems. This article investigates the multiconstraint operating regions of MMCs and the parameter influence on the common operating regions under grid phase disturbances. The multiconstraint operating regions under various phase differences between the grid voltage and the output of the PLL can be obtained by combining Lyapunov stability criteria, modulation index, and the maximum power transfer capability constraints. With the variation of phase differences, the multiconstraint operating regions tend to rotate in the *dq*-axis reference current coordinate plane. Besides, the common multiconstraint operating region can be affected by the parameters of the grid-connected MMC. The control parameters influence the multiconstraint operating region by changing the Lyapunov stability of the system, while the circuit parameters such as the resistance parameters, the inductance parameters, and the voltage parameters will also have an impact on the modulation boundary and the maximum power transfer boundary. Based on the operating region and the parameter analysis, the reference current limitation and the parameter adjustment are proposed as two effective methods to improve the stability of the system under grid phase disturbances. Three-phase 21-level MMC simulations and 5-level MMC HIL tests verify the operating regions and the stability improvement methods.

References

[1] C. K. Tse, M. Huang, X. Zhang, D. Liu, and X. L. Li, "Circuits and systems issues in power electronics penetrated power grid," *IEEE Open J. Circuits Syst.*, vol. 1, pp. 140–156, 2020.

[2] T. Ding *et al.*, "Quantifying cyber attacks on industrial MMC-HVDC control system using structured pseudospectrum," *IEEE Trans. Power Electron.*, vol. 36, no. 5, pp. 4915–4920, May 2021.

[3] J. Chivite-Zabalza, D. R. Trainer, J. C. Nicholls, and C. C. Davidson, "Balancing algorithm for a self-powered high-voltage switch using series-connected IGBTs for HVDC applications," *IEEE Trans. Power Electron.*, vol. 34, no. 9, pp. 8481–8490, Sep. 2019.

[4] S. Zhang *et al.*, "A monopolar symmetrical hybrid cascaded DC/DC converter for HVDC interconnections," *IEEE Trans. Power Electron.*, vol. 36, no. 1, pp. 248–262, Jan. 2021.

[5] C. Zou *et al.*, "Analysis of resonance between a VSC-HVDC converter and the ac grid," *IEEE Trans. Power Electron.*, vol. 33, no. 12, pp. 10157–10168, Dec. 2018.

[6] Y. Chen, M. Huang, S. Pan, A. El Aroudi, and X. Zha, "Transient voltage and current stresses estimation of MMC-MTDC system via discrete-time analysis," *IEEE Trans.Power Del.,* vol. 35, no. 6, pp. 2821–2830, Dec. 2020.

[7] L. Huang, H. Xin, and Z. Wang, "Damping low-frequency oscillations through VSC-HVDC stations operated as virtual synchronous machines," *IEEE Trans. Power Electron.,* vol. 34, no. 6, pp. 5803–5818, Jun. 2019.

[8] J. Khazaei, M. Beza, and M. Bongiorno, "Impedance analysis of modular multi-level converters connected to weak AC grids," *IEEE Trans. Power Syst.*, vol. 33, no. 4, pp. 4015–4025, Jul. 2018.

[9] J. Lyu, X. Zhang, X. Cai, and M. Molinas, "Harmonic state-space based small-signal impedance modeling of a modular multilevel converter with consideration of internal harmonic dynamics," *IEEE Trans. Power Electron.*, vol. 34, no. 3, pp. 2134–2148, Mar. 2019.

[10] J. Lyu, X. Cai, and M. Molinas, "Optimal design of controller parameters for improving the stability of MMC-HVDC for wind farm integration," *IEEE J. Emerg. Sel. Topics Power Electron.*, vol. 6, no. 1, pp. 40–53, Mar. 2018.

[11] J. Wang and P. Wang, "Decoupled power control for direct-modulation-based modular multilevel converter with improved stability," *IEEE Trans. Ind. Electron.*, vol. 66, no. 7, pp. 5264–5274, Jul. 2019.

[12] G. Bergna-Diaz, J. A. Suul, and S. D'Arco, "Energy-based state-space representation of modular multilevel converters with a constant equilibrium point in steady-state operation," *IEEE Trans. Power Electron.*, vol. 33, no. 6, pp. 4832–4851, Jun. 2018.

[13] D. Dong, B. Wen, P. Mattavelli, D. Boroyevich, and Y. Xue, "Grid-synchronization modeling and its stability analysis for multi-paralleled three-phase inverter systems," in *Proc. Annu. IEEE Appl. Power Electron. Conf. Expo.*, 2013, pp. 439–446.

[14] D. Dong, B. Wen, D. Boroyevich, P. Mattavelli, and Y. Xue, "Analysis of phase-locked loop low-frequency stability in three-phase grid-connected power converters considering impedance interactions," *IEEE Trans. Ind. Electron.*, vol. 62, no. 1, pp. 310–321, Jan. 2015.

[15] H. Wu and X. Wang, "Design-oriented transient stability analysis of grid-connected converters with power synchronization control," *IEEE Trans. Ind. Electron.*, vol. 66, no. 8, pp. 6473–6482, Aug. 2019.

[16] H. Wu and X. Wang, "Design-oriented transient stability analysis of PLL-synchronized voltage-source converters," *IEEE Trans. Power Electron.*, vol. 35, no. 4, pp. 3573–3589, Apr. 2020.

[17] X. He, H. Geng, R. Li, and B. C. Pal, "Transient stability analysis and enhancement of renewable energy conversion system during LVRT," *IEEE Trans. Sustain. Energ.*, vol. 11, no. 3, pp. 1612–1623, Jul. 2020.

[18] J. Zhao, M. Huang, H. Yan, C. K. Tse, and X. Zha, "Nonlinear and transient stability analysis of phase-locked loops in grid-connected converters," *IEEE Trans. Power Electron.*, vol. 36, no. 1, pp. 1018–1029, Jan. 2021.

[19] X. Fu *et al.*, "Large-signal stability of grid-forming and grid-following controls in voltage source converter: A comparative study," *IEEE Trans. Power Electron.*, vol. 36, no. 7, pp. 7832–78340, Jul. 2021.

[20] M. G. Taul, X. Wang, P. Davari, and F. Blaabjerg, "Robust fault ride through of converter-based generation during severe faults with phase jumps," *IEEE Trans. Ind. Appl.*, vol. 56, no. 1, pp. 570–583, Jan./Feb. 2020.

[21] D. S. d. S. Andrade, Y. N. Batista, F. A. S. Neves, and H. E. P. de Souza, "Fast phase angle jump estimation to improve the convergence time of the GDSC-PLL," *IEEE Trans. Ind. Electron.*, vol. 67, no. 4, pp. 2852–2862, Apr. 2020.

[22] X. Tian, W. Wang, X. Li, Y. Chi, Y. Li, and H. Tang, "Fault ride through strategy of DFIG using rotor voltage direct compensation control under voltage phase angle jump," *CSEE J. Power Energy Syst.*, vol. 5, no. 4, pp. 515–523, Dec. 2019.

[23] Ö. Göksu, R. Teodorescu, C. L. Bak, F. Iov, and P. C. Kjær, "Instability of wind turbine converters during current injection to low voltage grid faults and PLL frequency based stability solution," *IEEE Trans. Power Syst.*, vol. 29, no. 4, pp. 1683–1691, Jul. 2014.

[24] T. Li, A. M. Gole, and C. Zhao, "Harmonic instability in MMC-HVDC converters resulting from internal dynamics," *IEEE Trans. Power Del.,* vol. 31, no. 4, pp. 1738–1747, Aug. 2016.

[25] M. Saeedifard and R. Iravani, "Dynamic performance of a modular multilevel back-to-back HVDC system," *IEEE Trans. Power Del.*, vol. 25, no. 4, pp. 2903–2912, Oct. 2010.

[26] H. Yuan, X. Yuan, and J. Hu, "Modeling of grid-connected VSCs for power system small-signal stability analysis in DC-link voltage control timescale," *IEEE Trans. Power Syst.*, vol. 32, no. 5, pp. 3981–3991, Sep. 2017.

[27] Q. Tu and Z. Xu, "Impact of sampling frequency on harmonic distortion for modular multilevel converter," *IEEE Trans. Power Del.,* vol. 26, no. 1, pp. 298–306, Jan. 2011.

[28] Y. Liu, M. Huang, X. Zha, and H. H. C. Iu, "Short-circuit current estimation of modular multilevel converter using discrete-time modeling," *IEEE Trans. Power Electron.,* vol. 34, no. 1, pp. 40–45, Jan. 2019.

[29] L. Huang, H. Xin, Z. Wang, L. Zhang, K. Wu, and J. Hu, "Transient stability analysis and control design of droop-controlled voltage source converters considering current limitation," *IEEE Trans. Smart Grid*, vol. 10, no. 1, pp. 578–591, Jan. 2019.

Yushuang Liu (Student Member, IEEE) received the B.Eng. degree in electrical engineering in 2016 from Wuhan University, Wuhan, China, where she is currently working toward the Ph.D. degree.

From October 2019 to October 2020, she was a Visiting Ph.D. Student with the School of Electrical, Electronic and Computer Engineering, University of Western Australia, Perth, WA, Australia. Her main research interests focus on the modeling and stability analysis of power converters.

Meng Huang (Member, IEEE) received the B.Eng. and M.Eng. degrees from the Huazhong University of Science and Technology, Wuhan, China, in 2006 and 2008, respectively, and the Ph.D. degree from Hong Kong Polytechnic University, Hong Kong, in 2013.

He is currently an Associate Professor with the School of Electrical Engineering and Automation, Wuhan University, Wuhan, China. His research interest focuses on the nonlinear analysis of power converters and power electronics reliability.

Dr. Huang was a recipient of the Best Paper Award of the IEEE TRANSACTIONS ON POWER ELECTRONICS in 2016 and the Excellent Paper Award of the *CSEE Journal of Power and Energy Systems* in 2020. He serves as a Corresponding Guest Editor for the *IEEE Journal on Emerging and Selected Topics in Circuits and Systems*, the Guest Associate Editor for the IEEE JOURNAL OF EMERGING AND SELECTED TOPICS OF POWER ELECTRONICS, and an Associate Editor for IEEE ACCESS.

Chi K. Tse (Fellow, IEEE) received the B.Eng. (first-class hons.) and Ph.D. degrees from the University of Melbourne, Melbourne, VIC, Australia, in 1988 and 1991, respectively.

He is currently a Chair Professor of Electrical Engineering with the City University of Hong Kong, Hong Kong. Prior to joining City University, in October 2019, he was with Hong Kong Polytechnic University, Hong Kong, where he was the Head of the Department of Electronics and Information Engineering from 2005 to 2012 and a member of the University Council from 2013 to 2015. His research interests include complex network applications, power electronics, and nonlinear systems.

Dr. Tse was a recipient of several research and invention awards, including the IEEE TRANSACTIONS ON POWER ELECTRONICS Paper Prizes, Geneva International Invention Exhibition's Gold Medals, and Silicon Valley International Invention Festival's Grand Prize and Gold Medal. He serves and has served as the Editor-in-Chief for the IEEE TRANSACTIONS ON CIRCUITS AND SYSTEMS II, the *IEEE Circuits and Systems Magazine*, and the *IEICE Nonlinear Theory and Applications*, as an Editor for the *International Journal of Circuit Theory and Applications*, and an Associate Editor for a few other IEEE journals. He has been appointed to IEEE Distinguished Lecturer in 2005, 2010, and 2018 and to Honorary Professorship and Distinguished Fellowship by a few Australian, Canadian, and Chinese universities.

Herbert Ho-Ching Iu (Senior Member, IEEE) received the B.Eng. (hons.) degree in electrical and electronic engineering from the University of Hong Kong, Hong Kong, in 1997, and the Ph.D. degree in electronic and information engineering from Hong Kong Polytechnic University, Hong Kong, in 2000.

In 2002, he joined the School of Electrical, Electronic and Computer Engineering, The University of Western Australia, Perth, WA, Australia, where he is currently a Professor. His research interests include power electronics, renewable energy, nonlinear dynamics, current sensing techniques, and memristive systems.

Prof. Iu currently serves as an Associate Editor for the IEEE TRANSACTIONS ON POWER ELECTRONICS, IEEE TRANSACTIONS ON SMART GRIDS, IEEE TRANSACTIONS ON NETWORK SCIENCE AND ENGINEERING, and IEEE TRANSACTIONS ON CIRCUITS AND SYSTEMS—II.

Zhihong Yan (Student Member, IEEE) received the B.Eng. degree in electrical engineering from Wuhan University, Wuhan, China, in 2019. She is currently working toward the Ph.D. degree with the Department of Electrical and Electronics Engineering, The University of Hong Kong, Hong Kong.

Her current research interests include the modeling of reverse electrodialysis stacks, energy harvesting from salinity gradient power, maximum power tracking of renewable energy applications, and the modeling and stability analysis of power converters.

Xiaoming Zha (Member, IEEE) was born in Huaining, Anhui Province, China, in 1967. He received the B.S., M.S., and Ph.D. degrees in electrical engineering from Wuhan University, Wuhan, China, in 1989, 1992, and 2001, respectively.

He was a Postdoctoral Fellow with the University of Alberta, Canada, from 2001 to 2003. He has been a Faculty Member of Wuhan University since 1992 and became a Professor in 2003. He is currently the Deputy Dean with the School of Electrical Engineering, Wuhan University. His research interests include power electronic converter, the application of power electronics in smart grid and renewable energy generation, the analysis and control of microgrids, the analysis and control of power quality, and frequency control of high-voltage high-power electric motors.